Comparison of Structure and Reactivity of Hydrothermally Prepared Bi–Mo–Co–Fe–O Catalysts in Selective Propylene and Isobutene Oxidation

Linda Klag,[a] Lorena Baumgarten,[a, b] Abhijeet Gaur,[a] Thomas L. Sheppard+,[a, b] and Jan-Dierk Grunwaldt*[a, b]

The elucidation of structure-activity correlations in selective oxidation of propylene and isobutene over mixed metal oxides (MMO) is attractive for knowledge-based catalyst design and process optimisation. Particularly, 4-component Bi–Mo–Co–Fe–O catalysts need to be studied since their complex metal oxide phase mixture leads to higher activity and selectivity than 2-component Bi–Mo–O. Hence, three Bi–Mo–Co–Fe-oxides with different metal ratios were prepared by hydrothermal synthesis and compared during selective oxidation tests with propylene and isobutene. The active phases after several days on stream were investigated by synchrotron X-ray diffraction (XRD) and Raman spectroscopy, while the structural evolution under reaction conditions was followed by *operando* Raman spectroscopy, synchrotron XRD, and multi-

edge X-ray absorption spectroscopy. Similar structural transformations were observed during selective oxidation of propylene and isobutene, with similar influence on catalytic performance. A phase mixture of β-CoMoO$_4$/β-Co$_{0.7}$Fe$_{0.3}$MoO$_4$, γ-Bi$_2$MoO$_6$, Fe$_3$O$_4$ and Bi$_3$FeMo$_2$O$_{12}$ was observed, whereby high amounts of β-CoMoO$_4$/β-Co$_{0.7}$Fe$_{0.3}$MoO$_4$ increased selectivity to acrolein/methacrolein. In contrast, high amounts of γ-Bi$_2$MoO$_6$ and Fe$_3$O$_4$ favoured total oxidation to CO and CO$_2$. The simultaneous presence of β-CoMoO$_4$/β-Co$_{0.7}$Fe$_{0.3}$MoO$_4$, Bi$_3$FeMo$_2$O$_{12}$ and Fe$_2$O$_3$ increased selectivity to methacrolein in isobutene oxidation, whereas no comparative increase in acrolein selectivity was observed in propylene oxidation. This suggests different key active phases in both reactions.

Introduction

Bismuth molybdate based mixed metal oxide (MMO) catalysts are widely applied in chemical industry for selective oxidation of lower olefins, including conversion of propylene and isobutene to acrolein and methacrolein, respectively.[1–3] Although large-scale production of these important organic intermediates is well-established,[2,4] both processes involve high costs and excess CO$_2$ emissions with product yields well below 100%.[2] These drawbacks can be mitigated with better

understanding of the catalyst working principles and corresponding structure-activity correlations. These are still under debate,[5] although recent efforts have led to many new insights.[6–11] Bismuth molybdates, including the three main phases α-Bi$_2$Mo$_3$O$_{12}$, β-Bi$_2$Mo$_2$O$_9$ and γ-Bi$_2$MoO$_6$, are considered as key active phases, but their activity and selectivity trends have been inconsistently reported.[12–16] Moreover, their catalytic performance is strongly affected by further promoting phases such as Fe$_2$Mo$_3$O$_{12}$ and β-Co$_{0.7}$Fe$_{0.3}$MoO$_4$.[9,17] Generally, the catalytic performance of such multi-component systems (*e.g.*, Bi–Mo–Co–Fe–O) improves in comparison to the 2-component Bi–Mo-oxides,[9] motivating the use of complex MMO compositions on an industrial level (*e.g.*, Mo$_{12}$Bi$_{0.6}$Co$_7$Fe$_3$K$_{0.08}$Si$_{1.6}$O).[2,17–20] However, preparation (calcination, pH, precursor/metal ratios), activation or testing conditions (feed mixture, temperature, pressure) further strongly affect the formation of the corresponding metal oxide phases and thus, the overall catalytic performance.[21] Systematic approaches for deriving structure-activity correlations in multi-component systems are therefore crucial to understand the role of individual phases, but also their synergistic interplay and thus their working principles.

Common synthesis methods of Bi–Mo-based catalysts include co-precipitation,[22–23] spray drying,[24–25] or solid-state synthesis,[26] which all require harsh conditions and high calcination temperatures to obtain pure crystalline products. In this context, hydrothermal synthesis (HS) holds potential as a route to prepare nanostructured catalysts at lower temperatures.[27] The HS method is of particular interest to access materials of high crystallinity, high purity and controlled

[a]   L. Klag, L. Baumgarten, Dr. A. Gaur, PD Dr. T. L. Sheppard,+ Prof. Dr. J.-D. Grunwaldt
Institute for Chemical Technology and Polymer Chemistry (ITCP)
Karlsruhe Institute of Technology (KIT)
Engesserstraße 20
76131 Karlsruhe (Germany)
E-mail: grunwaldt@kit.edu

[b]   L. Baumgarten, PD Dr. T. L. Sheppard,+ Prof. Dr. J.-D. Grunwaldt
Institute of Catalysis Research and Technology (IKFT)
Karlsruhe Institute of Technology (KIT)
Hermann-von-Helmholtz Platz 1
76344 Eggenstein-Leopoldshafen (Germany)

[+]   Current address: Institute of Chemical Technology, Leipzig University, 04103 Leipzig, Germany.

morphology with high specific surface areas.[28–29] So far, the focus of HS was mainly on 2-component bismuth molybdates,[30–33] although extending HS towards more complex Bi–Mo–Co–Fe-oxides is both feasible and intriguing.

In general, the selective oxidation of lower olefins (*i.e.*, propylene and isobutene) is claimed to proceed in a similar manner.[2,34] To the best of our knowledge, only one systematic comparison of both reactions has been conducted,[35] referring to *ex situ* characterization of the catalysts. Systematic studies of this kind are useful for probing parallels and selectivity patterns in similar reactions, which may contribute to general rules for their working principles and thus ideally enhance their process efficiency. However, because the catalyst structure is highly dependent on the reaction conditions, it is crucial to monitor structural changes of Bi–Mo–Co–Fe-oxides by *in situ/operando* techniques.[36–37] Moreover, their complex composition requires a set of complementary characterization methods to fully deconvolute the various crystalline and amorphous metal oxide phases.[38]

In this work, we systematically investigate both the influence of the synthesis conditions during HS and compare propylene and isobutene as hydrocarbon reactants with respect to their catalytic performance (activity, selectivity) in lower olefin oxidation. Three Bi–Mo–Co–Fe-oxide catalysts with different elemental composition were synthesised and tested in a lab-scale unit for selective propylene and isobutene oxidation. For each reaction, the metal oxide composition before and after several days on stream was investigated by *ex situ* Raman spectroscopy and synchrotron X-ray diffraction (XRD). In addition, the structural evolution was monitored by *operando* Raman spectroscopy. Complementary insights were obtained by *operando* synchrotron XRD as well as element-specific and multi-edge X-ray absorption spectroscopy (XAS) in selective isobutene oxidation. The combination of structural insights with catalytic performance in selective propylene and isobutene oxidation aimed at a detailed understanding of metal oxide phase evolution and interplay under reaction conditions.

Results and Discussion

Ex Situ Characterization and Catalytic Testing

Three Bi–Mo–Co–Fe–O catalysts with different elemental compositions were prepared by HS at pH = 7, similar as described in previous work.[39] The targeted metal ratios refer to a higher amount of cobalt (HS–Co), iron (HS–Fe) and molybdenum (HS–U) within each system, whereby HS–U refers to an elemental composition firstly reported by Moro-Oka and Ueda (Table 1, entry 3) which is active and selective for propylene oxidation to acrolein.[9] The targeted and experimentally verified metal compositions (ICP-OES) are given in Table 1, showing that the targeted excess of either Co, Fe or Mo in each catalyst was obtained. Notably, HS–U and HS–Co exhibited significantly higher specific surface areas (A_{BET}, 81 and 89 m²/g,) compared to HS–Fe (48 m²/g, see Table 1), while all three were higher than those reported for similarly prepared Bi–Mo-oxides.[21,29,32]

The variations in catalyst composition further resulted in different metal oxide phases present, as detected by Raman spectroscopy (Figure 1a) and synchrotron XRD (Figure 1b). All three catalysts showed characteristic features assigned to β-CoMoO$_4$ and α-CoMoO$_4$. Moreover, XRD revealed the additional presence of γ-Bi$_2$MoO$_6$ in HS–U and HS–Co, while crystalline Fe$_3$O$_4$ was solely detected in HS–Co. Despite these differences, the catalysts showed relatively similar phase mixtures. Since the metal oxide phase formation in HS strongly depends on the applied conditions (*e.g.*, pH value),[21,39–41] the pH likely influenced the phase mixture more strongly than the specific metal ratios. Nevertheless, the phase mixtures present were not identical and consequently different catalytic behaviour was observed in selective olefin oxidation.

The results of catalytic testing in a lab-scale fixed-bed reactor are given in Figure 2. For better comparison between selective propylene (Figure 2a,b) and isobutene oxidation (Figure 2c,d), the catalysts were tested at similar WHSV (1.14 h^{-1} and 1.17 h^{-1}) but different oven temperatures in the range from 330–450 °C. In selective propylene oxidation, HS–U showed the most favourable combination of activity (X_{C3H6}~24%) and selectivity (S_{ACR}~78%) at 380 °C. At the same temperature, HS–Co and HS–Fe both showed similar but lower propylene conversion (X_{C3H6}~8%), with HS–Co acting more selective (S_{ACR} ~83%) than HS–Fe (S_{ACR} ~72%). For all catalysts, the by-products CO and CO$_2$ were detected, while acrylic acid was only measured over HS–U. This is most likely attributed to its relatively high propylene conversion, as acrylic acid was claimed to be formed consecutively from acrolein.[42–43] Notably, all three catalysts showed lower conversion (~8–35%) compared to a hydrothermally prepared Bi–Mo–Co–Fe-oxide reported in literature at same WHSV (X_{C3H6} ~63%).[44] Although all catalysts were prepared at pH = 7, which was found to improve catalytic performance of bismuth molybdate based systems in propylene oxidation,[21,39] the lower catalytic activity may be related to the differences in elemental composition and thus metal oxide

Table 1. Metal ratios as calculated (theoretical) and as determined by elemental analysis (ICP-OES) of HS catalysts with corresponding specific surface area (A_{BET}) as determined by N$_2$-physisorption.

Sample	Theoretical metal ratio/mol%				Metal ratio by ICP-OES/mol%				A_{BET}/m² g^{-1}
	Bi	Mo	Co	Fe	Bi	Mo	Co	Fe	
HS-Co	5.0	35.0	40.0	20.0	5.0 ± 0.1	33.8 ± 0.9	40.7 ± 0.8	20.5 ± 0.6	89
HS-Fe	5.0	35.0	20.0	40.0	5.2 ± 0.1	35.4 ± 0.9	17.7 ± 0.3	41.8 ± 1.1	48
HS-U	4.2	50.0	33.3	12.5	4.3 ± 0.1	45.9 ± 1.2	37.0 ± 0.7	12.7 ± 0.3	81
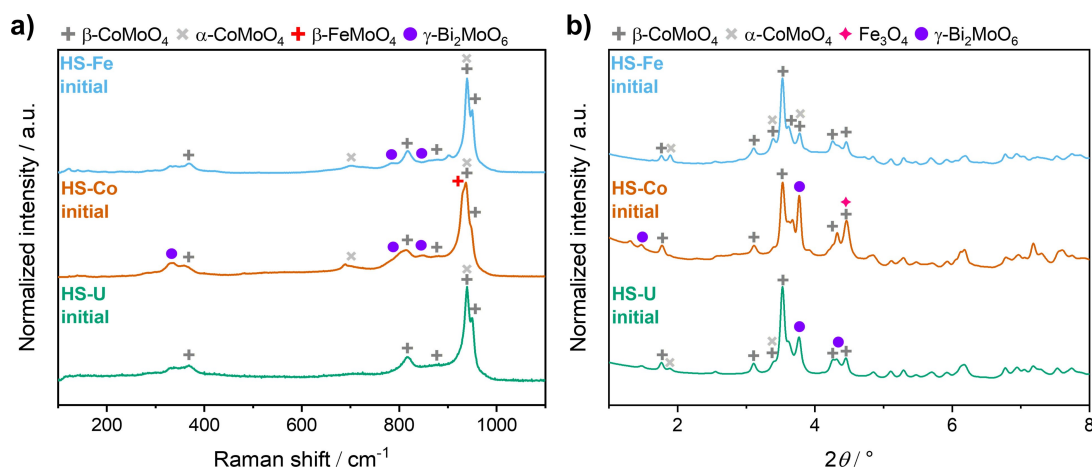
Figure 1. *Ex situ* Raman spectra (a) and synchrotron XRD patterns (b, $\lambda = 0.20735$ Å) of the hydrothermally prepared samples HS–U, HS–Co and HS–Fe after synthesis/before catalytic testing.
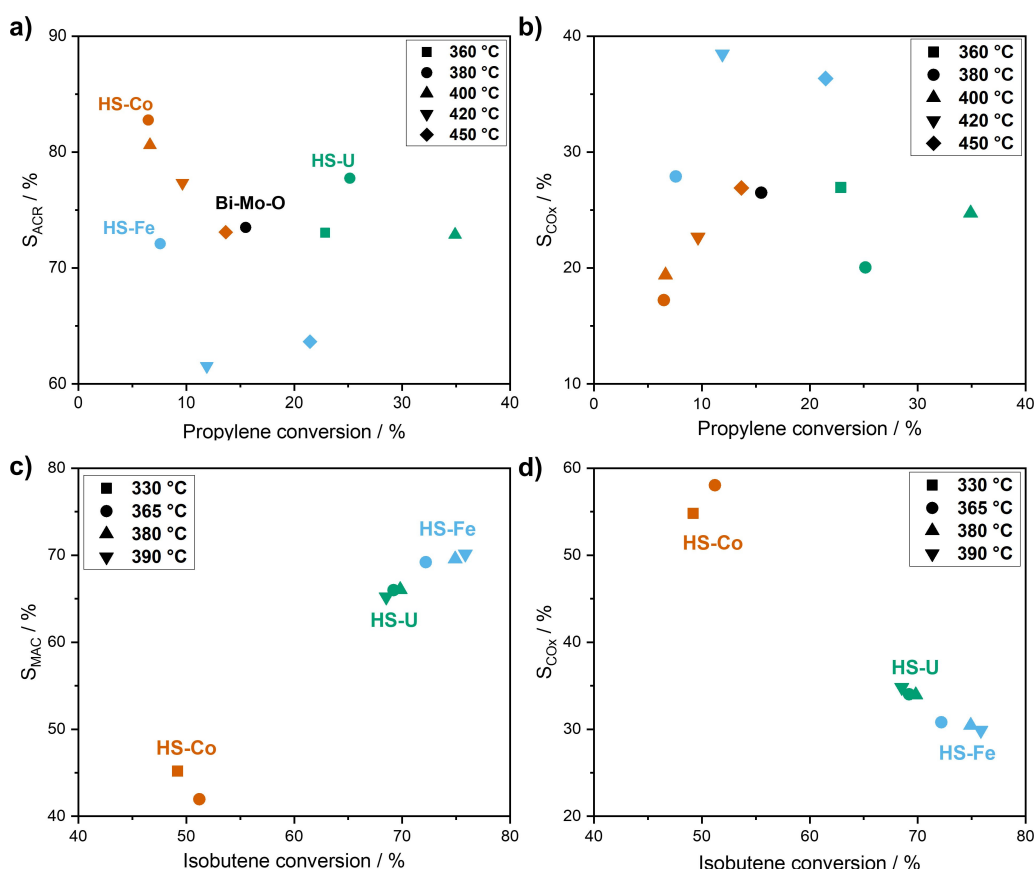
Figure 2. Conversion and selectivity of HS–U, HS–Co and HS–Fe in selective propylene (a, b) and isobutene oxidation (c, d) measured in reaction atmosphere ($N_2/O_2/C_nH_{2n}/H_2O = 70/14/8/8$ vol%) at oven temperatures in a range of 330–450 °C at similar WHSV (1.14 and 1.17 h^{-1}). Additionally, a comparison to hydrothermally prepared 2-component Bi–Mo–O in propylene oxidation[45] is shown in a,b.

phases. Moreover, the strong pH sensitivity of this preparation method can easily induce pronounced changes in catalytic performance. Notably, the selectivity of HS–Co was similar to hydrothermally synthesized Bi–Mo-oxides in propylene oxidation[45] at comparable conditions (Figure 2a,b), while HS–Fe performed even less selective. This strongly emphasizes that the addition of cobalt and iron to pure Bi–Mo–O systems is

only beneficial in a certain ratio, while phase cooperation of certain metal oxides is a more important factor in catalytic activity and selectivity.

As A_{BET} of all catalysts (Table 1) were higher compared to previous studies, this further indicates a less important role of the specific surface area compared to phase composition and/ or cooperation. This is in line with previous observations in

ChemCatChem

Research Article
doi.org/10.1002/cctc.202301470

**Chemistry
Europe**
European Chemical
Societies Publishing

selective olefin oxidation over Bi–Mo–Co–Fe–O, where a decrease in surface area was observed with time on stream at nearly constant and high olefin conversion.[36–37]

Altered trends in catalytic performance were observed during selective oxidation of isobutene. Generally, the oxidation rates were much higher. HS–Fe revealed highest activity (X_{C4H8}~72–75%) and selectivity (S_{MAC}~68–70%), followed by HS–U (X_{C4H8}~68–70%, S_{MAC}~65–66%) and HS–Co (X_{C4H8}~48–51%, S_{MAC}~43-45%). Other by-products included CO and CO_2, and no significant amounts of methacrylic acid. Once ignited, the catalytic performance did not change significantly with temperature and all catalysts operated close to full oxygen consumption. This is related to a generally higher reactivity of isobutene compared to propylene and can be counteracted by a strong dilution of the catalysts without changes in activity and selectivity trends. However, for direct comparison of both olefins, the testing parameters were kept similar (*e.g.*, same catalyst masses). While the generally higher activity found in isobutene oxidation is most likely related to its additional methyl group, the different selectivity trends found for both reactions might indicate different roles of the individual metal oxide phases in either selective propylene or isobutene oxidation.

For direct comparison of the metal oxide phase composition after several days on stream, HS–Co, HS–Fe and HS–U were further characterised by Raman spectroscopy (Figure 3a,b) and synchrotron XRD (Figure 3c,d) after each catalytic reaction. Qualitatively, the same metal oxide phases were detected within each system after both selective propylene and isobutene oxidation. In fact, HS–U and HS–Co both showed phase mixtures containing β-CoMoO$_4$, α-CoMoO$_4$, γ-Bi$_2$MoO$_6$, Bi$_3$FeMo$_2$O$_{12}$ and Fe$_3$O$_4$. HS–Fe qualitatively contained the same metal oxides excluding γ-Bi$_2$MoO$_6$. Instead, Fe$_2$O$_3$ was detected solely in HS–Fe after each reaction.

Despite their qualitatively similar phase composition, pronounced quantitative differences were found with respect to the crystalline phase amounts in HS–Co, HS–Fe and HS–U, as determined by Rietveld refinement (Table 2). For example, a large fraction of crystalline Fe$_2$O$_3$ was detected in HS–Fe, while HS–Co and HS–U contained the highest amount of β-CoMoO$_4$, again with a significantly higher amount of Fe$_3$O$_4$ in HS–Co. α-CoMoO$_4$, Bi$_3$FeMo$_2$O$_{12}$ and γ-Bi$_2$MoO$_6$ rather represented minor phases ($<$10 wt%), with the first two metal oxides being present in all three catalysts, while the latter was not detected in HS–Fe. Similar trends were found for selective propylene and isobutene oxidation, but the absolute phase amounts partly differed (Table 2).
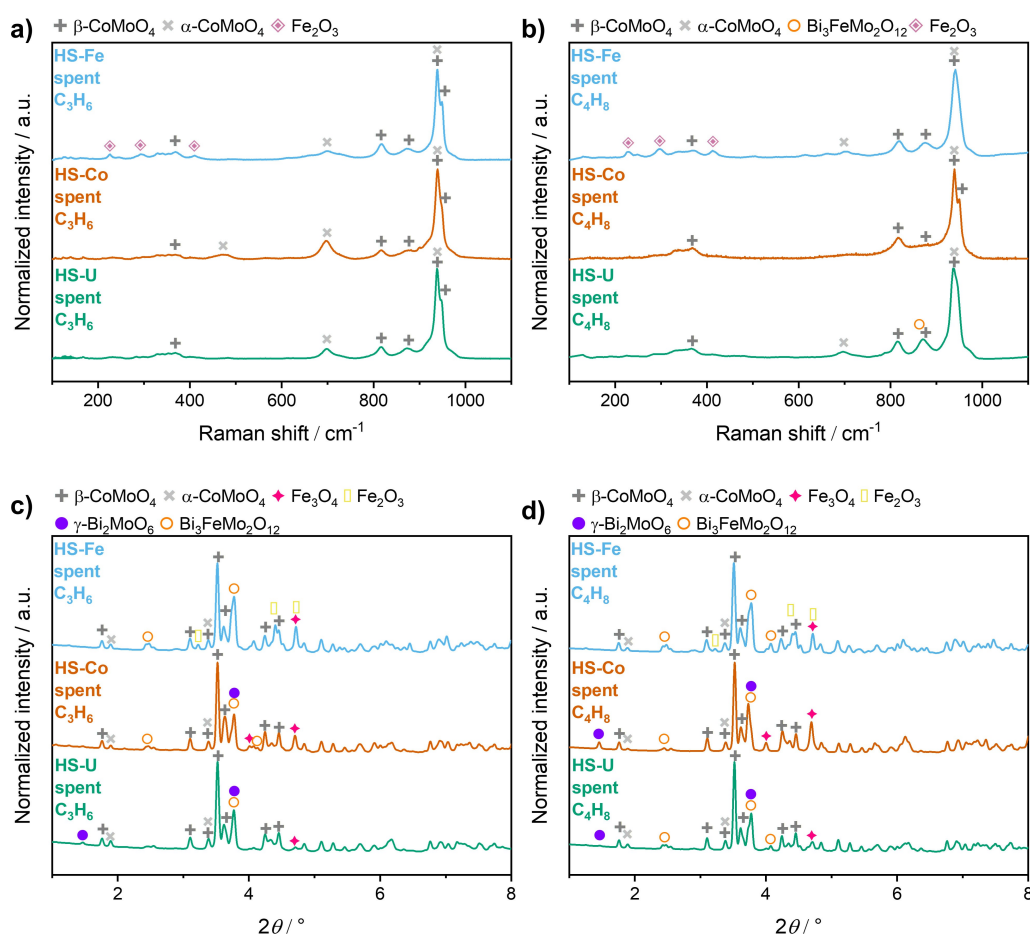
Figure 3. *Ex situ* Raman spectra (a, b) and synchrotron XRD patterns (c, d, λ=0.20735 Å) of the hydrothermally prepared samples HS–U, HS–Co and HS–Fe after catalytic testing in selective propylene (a, c) and isobutene (b, d) oxidation.

ChemCatChem

Research Article
doi.org/10.1002/cctc.202301470

Chemistry
Europe
European Chemical
Societies Publishing

Table 2. Overview of crystalline phases and phase fractions of HS–Co, HS–Fe and HS–U as determined by Rietveld refinement after catalytic testing in selective propylene (C_3H_6) and isobutene (C_4H_8) oxidation. A detailed description of the fit results is given in the ESI, section 4.1.

Crystalline phases via Rietveld refinement	Phase composition via Rietveld refinement/wt%					
	HS-Co		HS-Fe		HS-U	
	C_3H_6	C_4H_8	C_3H_6	C_4H_8	C_3H_6	C_4H_8
β-$CoMoO_4$	70.2	60.5	27.4	37.0	77.7	70.3
α-$CoMoO_4$	4.3	2.5	2.5	2.2	9.0	5.0
Fe_2O_3	–	–	57.5	48.3	–	–
Fe_3O_4	14.5	26.7	5.9	4.8	4.3	13.8
$Bi_3FeMo_2O_{12}$	9.5	2.1	6.8	7.7	4.5	8.9
γ-Bi_2MoO_6	1.5	8.2	–	–	4.6	2.0

This observation may be attributed to several reasons. First, metal oxide phase transformations strongly depend on the applied reaction conditions, such as temperature and gas atmosphere. Even though the chosen gas mixture only differed in the hydrocarbon reactant, this resulted in e.g., different oven temperatures needed for the ignition of the reaction or also in the catalyst bed, so that the catalysts were exposed to different temperature programs. Apart from that, the catalysts were characterised after similar time on stream, but an identical sample with respect to the catalyst bed position could not be guaranteed. Moreover, local heterogeneities in hydrothermally prepared MMO are likely,[44] but cannot be investigated in detail by Raman spectroscopy and XRD on powders, as both techniques typically provide global data over the whole catalyst bed. In other words, structural gradients along the catalyst bed or within the particles can occur apart from the structural changes taking place under reaction conditions. Hence, structural changes were next monitored by temperature-programmed *operando* Raman spectroscopy experiments in the middle of the catalyst bed in a microreactor. This allows to investigate the influence of the elemental composition of the hydrothermally prepared catalysts together with their phase evolution in both selective propylene and isobutene oxidation under more comparable conditions.

Operando Raman Spectroscopy in Selective Propylene and Isobutene Oxidation
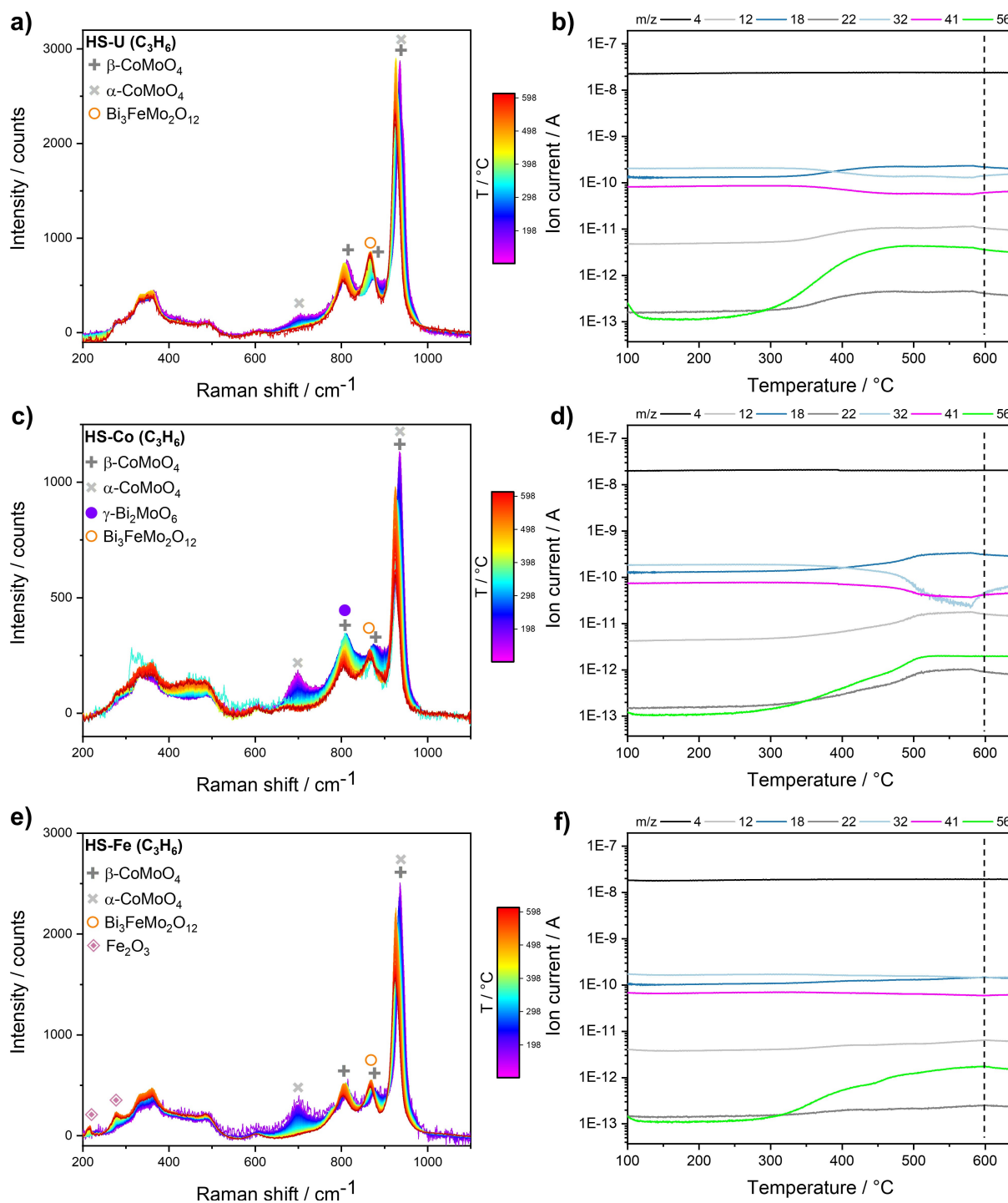
As indicated by *ex situ* characterization, the qualitative phase mixtures of HS–U, HS–Fe and HS–Co were found to be similar during reaction, although catalytic performance differed according to temperature and feedstock. To further unravel structural changes in each system, *operando* Raman spectroscopy during temperature-programmed reaction in propylene and isobutene was performed (Figures 4 and 5, respectively).

Similar to the results in the lab-scale testing unit, HS–Fe showed poorest catalytic performance during selective propylene oxidation in the microreactor (Figure 4f), while HS–U performed best in terms of propylene conversion and acrolein selectivity (Figure 4b). Both catalysts contained β-$CoMoO_4$ and α-$CoMoO_4$, together with an increased formation of $Bi_3FeMo_2O_{12}$

at higher temperatures (Figure 4a,e). Notably, the initial characteristic band of α-$CoMoO_4$ was more pronounced for HS–Fe, while a more pronounced band of Bi_3FeMoO_{12} was detected for HS–U. Since $Bi_3FeMo_2O_{12}$ is assumed to perform selectively in lower olefin oxidation and octahedrally coordinated molybdenum (e.g., α-$CoMoO_4$) favours total oxidation, these results are in good agreement with literature.[8,36,46] However, not only the presence of phases but also phase cooperation as well as inactive or non-selective phases must be considered. For example, the additional presence of Fe_2O_3 was only observed in the case of HS–Fe and is most likely the origin of its low catalytic activity in propylene oxidation, as the iron redox couple Fe^{2+}/Fe^{3+} is known to be crucial in the catalytic cycle.[9,36–37,47–48] Hence, reducible Fe^{3+} species were barely available within Fe_2O_3 in selective propylene oxidation over Bi–Mo–Co–Fe-oxides.

Notably, HS–Co showed higher conversion in the microreactor compared to HS–U (Figure 4b,d), in contrast to the lab-scale testing unit results (Figure 2a). The high catalytic activity was accompanied by high oxygen conversion, which even exceeded propylene conversion in the temperature range of ~510–595 °C. Almost total oxygen consumption was also observed in our previous study, involving simultaneous presence of γ-Bi_2MoO_6 and Fe_3O_4 in Bi–Mo–Co–Fe-oxides.[37] Here, γ-Bi_2MoO_6 was solely detected by Raman spectroscopy in HS–Co, while *ex situ* XRD after several days on stream further confirmed the presence of Fe_3O_4 (Figure 3c). Consequently, this further strengthens the assumption that the synergistic interplay of γ-Bi_2MoO_6 and Fe_3O_4 results in high oxygen consumption and promotes overoxidation to CO and CO_2. At higher temperatures (>595 °C), a decrease in MS signals without a pronounced shift in the Raman spectra was observed. Instead, a decrease of the intensity of all metal oxide signals was detected, which might be attributed to the formation of carbon species due to high temperatures and/or low oxygen content in the gas mixture. Such carbon formation was also reported for Bi–Mo-oxides in reducing propylene atmosphere.[45]

During selective isobutene oxidation, all three catalysts exhibited generally higher olefin conversion compared to propylene oxidation when using the same catalyst mass and WHSV (Figure 5b,d,f). The experiments in the microreactor revealed the same trends as in the lab-scale testing unit and

ChemCatChem

Research Article
doi.org/10.1002/cctc.202301470

**Chemistry
Europe**
European Chemical
Societies Publishing

Figure 4. Series of overlaid Raman spectra together with simultaneously acquired MS data during temperature-programmed reaction in propylene (100–600 °C, 2 °C/min, $He/O_2/C_3H_6/H_2O = 70/14/8/8$ vol.%) over HS–U (a,b), HS–Co (c,d) and HS–Fe (e,f). Dotted vertical lines indicate the start of the isothermal period at 600 °C (15 min). MS signals refer to unique fragments of each species with m/z: 4: He, 12: CO, 18: H_2O, 22: CO/CO_2, 32: O_2, 41: C_3H_6, 56: C_3H_4O.

structural changes of HS–U, HS–Co and HS–Fe during selective isobutene oxidation were very similar to those in selective propylene oxidation (Figure 5a,c,e).

For better comparison, selected Raman spectra acquired at the same temperatures (200, 400 and 600 °C) during both reactions were compared after normalization (ESI, section 5) and revealed the same band positions at each temperature within each catalyst. Notably, the main band intensity corresponding to β-CoMoO$_4$ (~936 cm^{-1}) decreased at lower temperatures compared to selective propylene oxidation. Similar to the observations in propylene oxidation over HS–Co, this pronounced decrease of Raman signal intensity particularly over HS–Co and HS–U in isobutene oxidation was accompanied by high oxygen consumption. Since no band stemming from metal
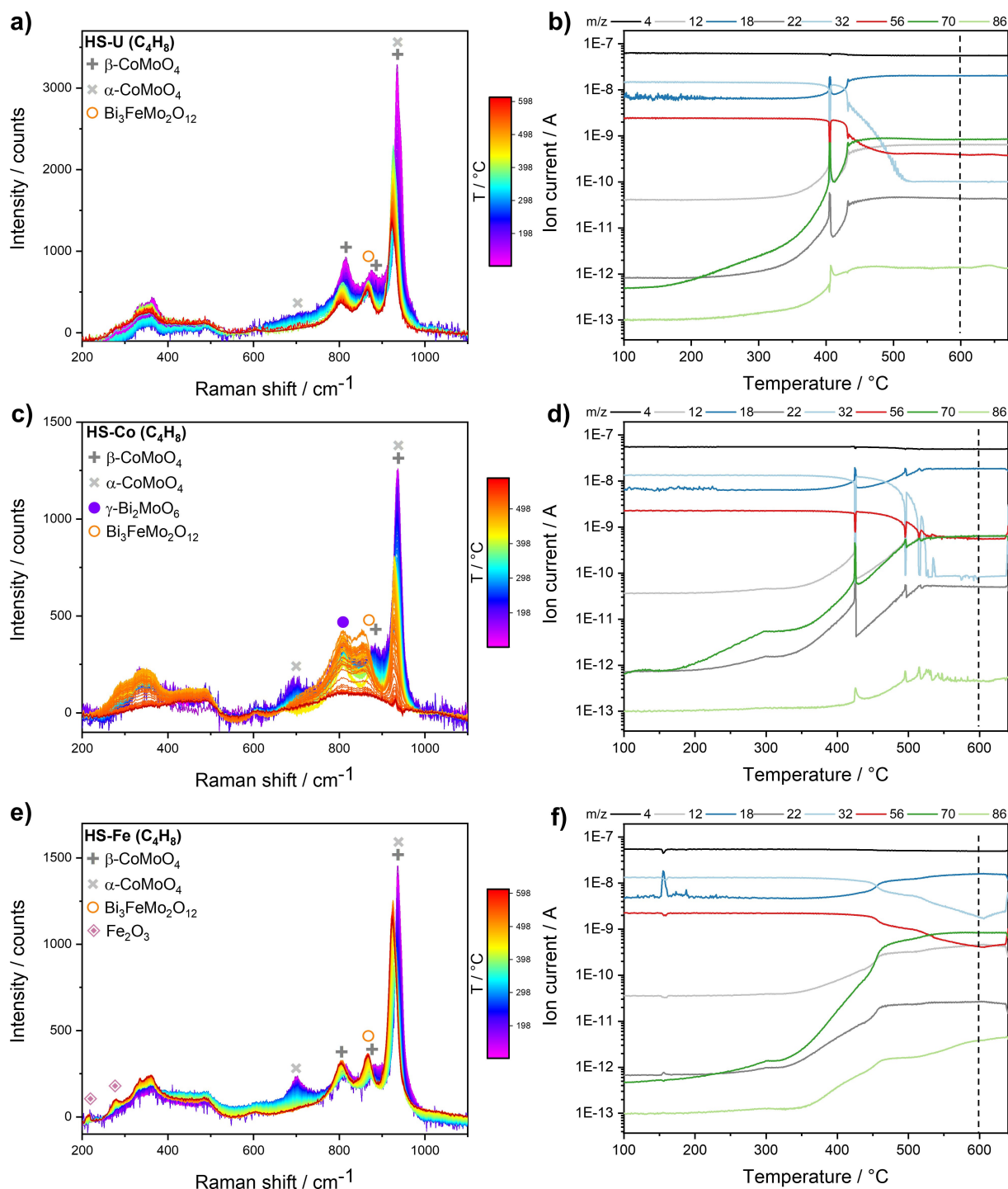
Figure 5. Series of overlaid Raman spectra together with simultaneously acquired MS data during temperature-programmed reaction in isobutene (100–600 °C, 2 °C/min, He/O$_2$/C$_4$H$_8$/H$_2$O = 70/14/8/8 vol.%) over HS–U (a,b), HS–Co (c,d) and HS–Fe (e,f). Dotted vertical lines indicate the start of the isothermal period at 600 °C (15 min). MS signals refer to unique fragments of each species with m/z: 4: He, 12: CO, 18: H$_2$O, 22: CO/CO$_2$, 32: O$_2$, 56: C$_4$H$_8$, 70: C$_4$H$_6$O, 86: C$_4$H$_6$O$_2$.

oxide vibrations could be detected for HS–Co at ~600 °C anymore, this indicates that the catalyst was covered by carbonaceous species. Carbon formation seems to be enhanced by the tendency of HS–Co towards total oxidation in both selective propylene and isobutene oxidation and thus some oxygen deficiency downstream of the catalyst bed. Moreover,

the higher conversion of isobutene compared to propylene likely caused a higher heat release in the microreactor further favouring carbon formation.

Remarkably, HS–Fe showed similar isobutene conversion as HS–Co but at more moderate oxygen consumption. Since also methacrolein formation was found higher in HS–Fe, this

ChemCatChem

Research Article
doi.org/10.1002/cctc.202301470

Chemistry
Europe

European Chemical
Societies Publishing

revealed again the same trend as in the lab-scale testing results, with HS–Fe showing best performance among the three catalysts in selective isobutene oxidation. This differs from the catalytic behaviour of HS–Fe in selective propylene oxidation (*i.e.*, low propylene conversion and acrolein selectivity) and might suggest an alternative key active phase or at least a partly different role of iron in both reactions.

Operando synchrotron XRD in selective isobutene oxidation

As qualitatively similar structural changes were found with *operando* Raman spectroscopy in both reactions, complementary *operando* synchrotron XRD of HS–Co, HS–Fe and HS–U was performed to further unravel the evolution of the crystalline metal oxide phases during selective oxidation of isobutene at high resolution (Figure 6). This reaction generally revealed a higher reactivity, and thus more detailed insights into the dynamic catalytic processes over Bi–Mo–Co–Fe–O are needed. *Operando* XRD during temperature-programmed reaction in isobutene was performed in combination with sequential Rietveld refinement, which gave additional and precise insights in terms of crystalline metal oxide phase composition and phase amounts, along with information on the microstructure (*i.e.*, crystallite size).

The XRD patterns acquired in reaction atmosphere at $100\,°C$ revealed the same initial phase mixtures as found by *ex situ* synchrotron XRD prior to reaction (Figure 1b). Rietveld refinement revealed largest fractions of β-CoMoO$_4$ in all three catalysts, but the other phases present differed between the catalysts (Figure 7). HS–Fe contained a relatively large amount of α-CoMoO$_4$ (~23 wt%) compared to HS–U (~9 wt%). In turn, HS–U additionally contained γ-Bi$_2$MoO$_6$ (~7 wt%) which was also detected at higher amount (~13 wt%) and in conjunction with Fe$_3$O$_4$ (~14 wt%) in HS–Co. As discussed previously, the combination of γ-Bi$_2$MoO$_6$ and Fe$_3$O$_4$ is most likely the origin of high catalytic activity and oxygen consumption leading to CO and CO$_2$ formation. Notably, both crystalline γ-Bi$_2$MoO$_6$ and Fe$_3$O$_4$ were also detected in HS–U after ignition of the reaction, emphasizing the importance of the metal oxide phase amounts. Especially the amount of Fe$_3$O$_4$ was found significantly higher in HS–Co (~32 wt%) than in HS–U (7-9 wt%), likely causing overoxidation as it contains easily accessible oxygen. Moreover, the crystallite sizes of Fe$_3$O$_4$ were found comparably small (HS–Co: ~13–18 nm, HS–U: 4–16 nm) to those of the other metal oxides and remained in a stable range over the entire temperature program. This could further contribute to the high catalytic activity. At the same time, the amount of γ-Bi$_2$MoO$_6$ in HS–U

decreased upon ignition of the reaction, while that of Bi$_3$FeMo$_2$O$_{12}$ increased resulting in higher methacrolein selectivity. This supports our observations with *operando* Raman spectroscopy.
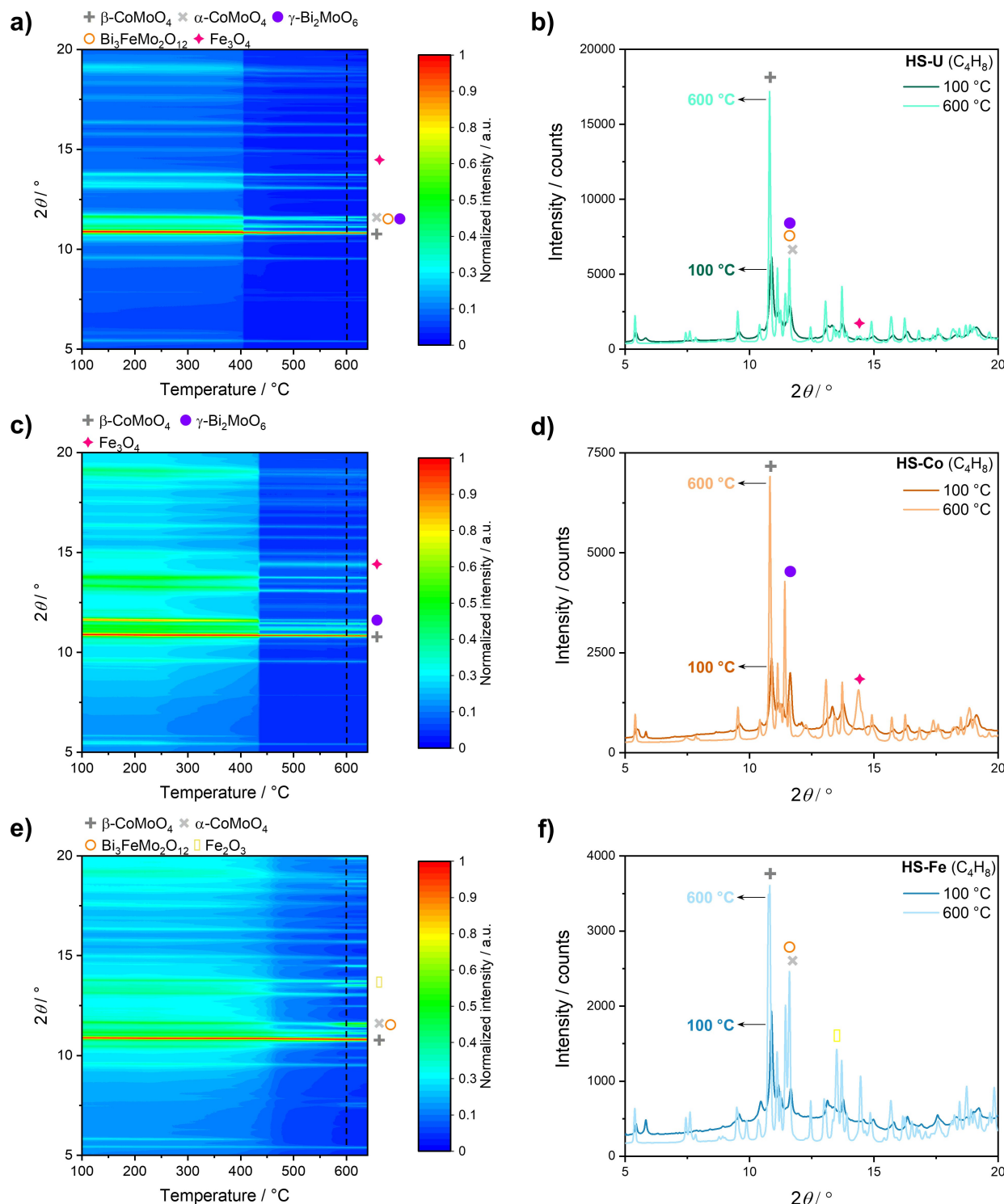
For HS–Fe, the ignition of the reaction and crystalline structural changes were shifted to higher temperatures. This might be attributed to the lower A$_{BET}$ measured for HS–Fe, which is also indicated by the slightly higher crystallite sizes of β-CoMoO$_4$ and α-CoMoO$_4$ (~33 and 26 nm) in HS–Fe compared to HS–U (~25 and 22 nm) and HS–Co (~27 nm). Further, it may be related to the absence of Fe$_3$O$_4$ and Bi$_3$FeMo$_2$O$_{12}$.

Upon ignition of the reaction, α-CoMoO$_4$ fully transformed to β-CoMoO$_4$. Notably, this transformation was slower than the structural transformations in HS–Co and HS–U, which is likely related to the lower reactivity and higher selectivity of HS–Fe to methacrolein with lower heat release compared to total oxidation. Crystalline Fe$_2$O$_3$ and Bi$_3$FeMo$_2$O$_{12}$ were detected starting from ~500$\,°C$, but were present as amorphous phases already below 500$\,°C$ as seen by Raman spectroscopy (Figure 5e). The amount of crystalline Bi$_3$FeMo$_2$O$_{12}$ was found higher in HS–Fe (~13 wt%) than in HS–Co (no crystalline Bi$_3$FeMo$_2$O$_{12}$ detected during TPRxn), which probably contributed to its highest methacrolein selectivity. At the same time, a large fraction of Fe$_2$O$_3$ (~25 wt%) was detected in HS–Fe, which in contrast to the high amount of Fe$_3$O$_4$ in HS–Co (~31 wt%) did not result in overoxidation. Hence, either solely the interplay of γ-Bi$_2$MoO$_6$ and Fe$_3$O$_4$ results in enhanced CO$_x$ formation, or rather single metal oxide spinel-type structures (*i.e.*, Fe$_3$O$_4$) are the origin of total oxidation. This might be due to the presence of the iron redox couple within Fe$_3$O$_4$, while Fe$_2$O$_3$ solely provides less dynamic Fe^{3+}. Consequently, the selective oxidation of isobutene seems to perform well over Fe^{3+}, as present in Fe$_2$O$_3$ but also within Bi$_3$FeMo$_2$O$_{12}$, while the activation of propylene seems to particularly require the reduction from Fe^{3+} to Fe^{2+} or a higher electron/oxygen mobility within the lattice. Moreover, no pure bismuth molybdate phase (α-, β- or γ-phase) was detected by *operando* Raman spectroscopy or synchrotron XRD over active and selective HS–Fe in isobutene oxidation. This could further indicate, that pure bismuth molybdates are contrarily to propylene oxidation not required in isobutene oxidation, but instead could be taken over by Bi$_3$FeMo$_2$O$_{12}$. At the same time, Bi$_3$FeMo$_2$O$_{12}$ might have been formed from a bismuth molybdate phase, not detected by the herein applied characterization techniques. Sleight and Jeitschko[49] reported on Bi$_3$FeMo$_2$O$_{12}$ synthesis directly from a mixture of aqueous solutions of ferric nitrate, bismuth nitrate and ammonium molybdate, and thus from similar precursors as used in this study (Table 3). Hence, this strengthens the assumption of

Table 3. Metal ratios (as calculated) and precursor masses used for HS.

Sample	Metal ratio/mol%				Precursor mass/g			
	Bi	Mo	Co	Fe	Bi(NO$_3$)·6 H$_2$O	(NH$_4$)$_6$Mo$_7$O$_{24}$·4 H$_2$O	Co(NO$_3$)$_2$·6 H$_2$O	Fe(NO$_3$)$_2$·9 H$_2$O
HS–Co	5.0	35.0	40.0	20.0	0.89	2.3	5.33	2.97
HS–Fe	5.0	35.0	20.0	40.0	0.89	2.8	2.27	5.96
HS–U	4.2	50.0	33.3	12.5	0.72	3.8	3.76	1.77

ChemCatChem

Research Article
doi.org/10.1002/cctc.202301470

Chemistry Europe
European Chemical
Societies Publishing

Figure 6. Normalized 2D XRD patterns (left) and selected XRD patterns (recorded at beamline BM01 at ESRF, $\lambda = 0.63988$ Å) at 100 °C and 600 °C (right) of HS–U (a,b), HS–Co (c,d) and HS–Fe (e,f) with the assignment of the main reflections of the present metal oxide phases during temperature-programmed reaction in isobutene (100-600 °C, 2 °C/min, He/O$_2$/C$_4$H$_8$/H$_2$O = 70/14/8/8 vol.%). Dotted vertical lines indicate the start of the isothermal period at 600 °C (15 min).

Bi$_3$FeMo$_2$O$_{12}$ acting as key active and/or selective phase in selective isobutene oxidation. For a deeper understanding of the roles of the individual metals and their reaction behaviour, further *operando* characterization was conducted by XAS in selective isobutene oxidation.

Complementary characterization of HS-U by *operando* XAS in selective isobutene oxidation

For more detailed insights into the structural changes of the individual metals, element-specific XANES and EXAFS spectra at
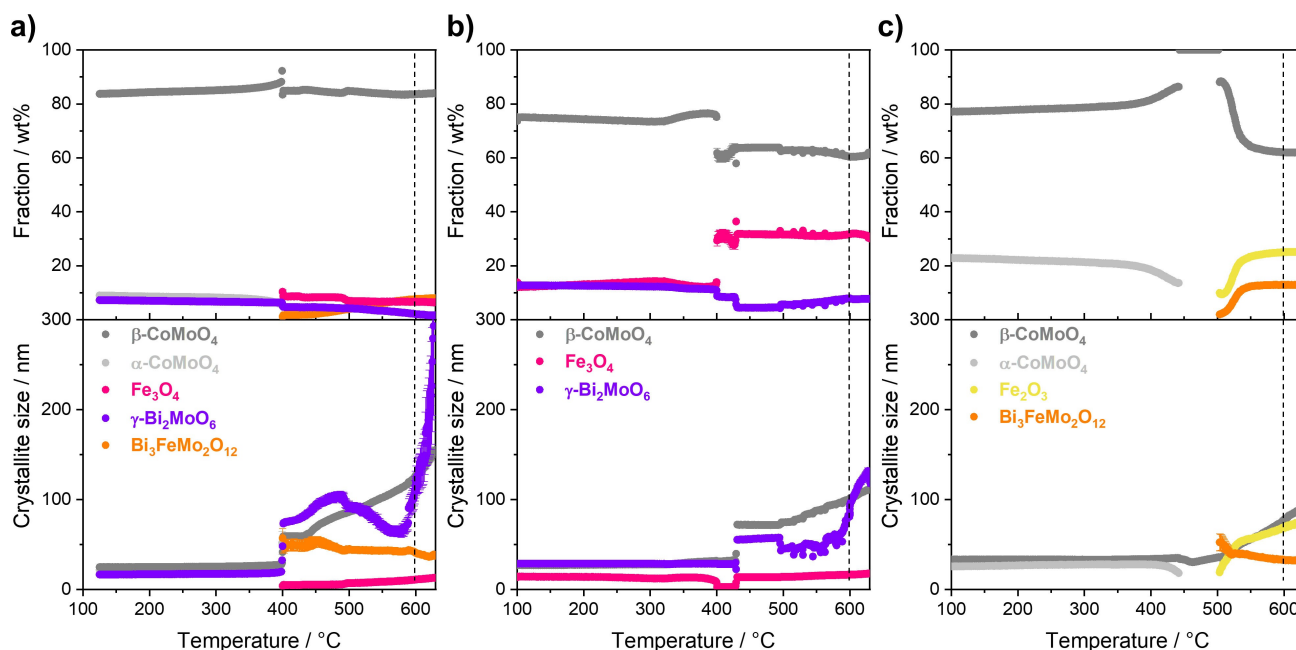
Figure 7. Evolvement of crystalline phases (top) and crystallite sizes (bottom) derived from synchrotron XRD ($\lambda = 0.63988$ Å) with Rietveld refinement of HS–U (a), HS–Co (b) and HS–Fe (c) during temperature-programmed reaction in isobutene (100-600 °C, 2 °C/min, He/O$_2$/C$_4$H$_8$/H$_2$O = 70/14/8/8 vol.%). Dotted vertical lines indicate the start of the isothermal period at 600 °C (15 min). A detailed description of the fit results is given in the ESI, section 4.2.
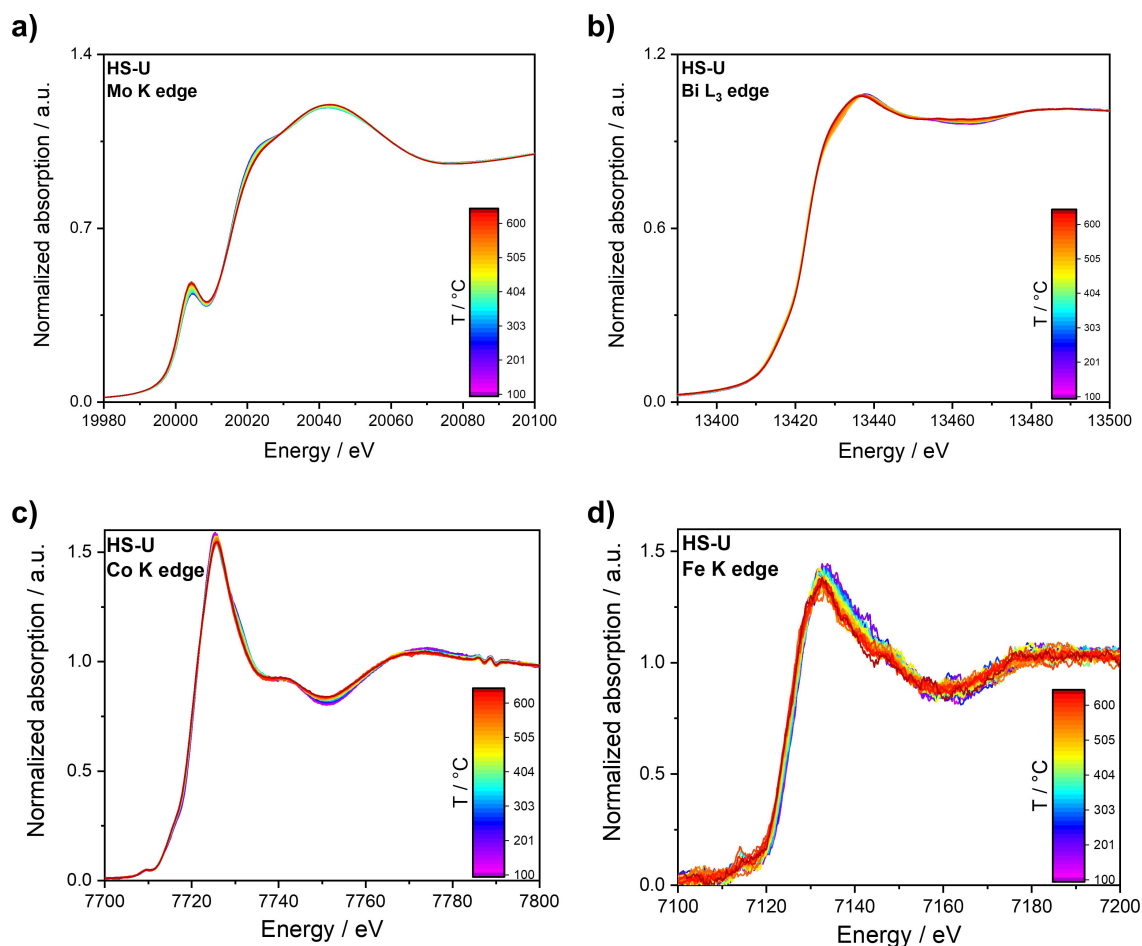
Mo K-, Bi L$_3$-, Co K- and Fe K-edges were recorded for HS–U during selective isobutene oxidation (Figure 8). HS–U contained the greatest variety in phase mixture and showed comparably high conversion with relatively high acrolein or methacrolein selectivity in both reactions.

At Mo K-edge, an increase in the pre-edge feature together with a shift of the feature at ~20027 eV indicated an increase in the tetrahedral nature of Mo with increasing temperature. This could be attributed on the one hand to the transformation of α- to β-CoMoO$_4$, which was also confirmed at Co K-edge by the shift of the feature at ~7732 eV to lower energies.[50] On the other hand, the spectra at Bi L$_3$-edge showed an increased contribution of scheelite-type Bi$_3$FeMo$_2$O$_{12}$ at higher temperatures. These results are in good agreement with the complementary Raman spectroscopy and XRD data.

In addition, a comparably high contribution of Bi$_3$FeMo$_2$O$_{12}$ was already detected in the initial state of HS–U by linear combination fitting (LCF) at Bi L$_3$-edge (see ESI, section 6), indicating that Bi$_3$FeMo$_2$O$_{12}$ was likely formed during the catalyst synthesis. This further indicates that the above discussed formation of Bi$_3$FeMo$_2$O$_{12}$ in HS–Fe probably took place during HS as well. Besides, LCF of the spectra at Fe K-edge revealed a mixture of Fe$_2$O$_3$ and Fe$_3$O$_4$, and thus a mixture of octahedrally and tetrahedrally coordinated Fe^{3+} and Fe^{2+}, with increasing contribution of Fe$_3$O$_4$ at higher temperatures. Such an increase was also observed on other Bi–Mo–Co–Fe–O catalysts with XAS in a previous study.[37] In this context, a constant presence of Fe$_3$O$_4$ without full iron reduction to Fe^{2+} went along with high isobutene conversion and high oxygen consumption, as also seen for HS–U. Overall, *operando* XAS of HS–U revealed the most pronounced element-specific changes

for Fe and Mo, while Bi and Co remained rather stable. Such a dynamic change of Fe and Mo has also been observed on the multicomponent system in selective propylene oxidation.[18,36]

In the end, the metal oxide phase mixtures of HS–U, HS–Co and HS–Fe were qualitatively the same after each reaction, but different selectivity trends were found particularly for HS–Fe. This is highlighted schematically in Figure 9. Moreover, higher olefin conversions were observed in selective isobutene oxidation. This suggests a generally higher reactivity of isobutene due to its additional methyl group. Although quantitative differences were observed within each system after the respective olefin oxidation for several days on stream, these were most likely linked to the catalytic behaviour of each hydrocarbon. For example, the generally higher conversions of isobutene probably went along with a higher heat release, which in turn can directly affect the metal oxide structures (*e.g.*, crystallisation, sintering, composite formation). Hence, such quantitative differences in the metal oxides could hardly be avoided within this study, which aimed for measuring both reactions under similar reaction conditions. For more insights into the influence of released temperature on catalyst structure, spatially-resolved techniques are a promising approach. These allow to investigate temperature, structure and concentration gradients along the catalyst bed within a single experiment.[51–54] In this context, the dynamics of the catalytic processes need to be further addressed in future studies, involving characterization on several time and length scales.[38] This includes for example complementary insights into the surface layer of the catalysts, which are equally important to the herein conducted bulk experiments.

ChemCatChem

Research Article
doi.org/10.1002/cctc.202301470

Chemistry Europe
European Chemical
Societies Publishing

Figure 8. Normalized XANES spectra of HS–U acquired during temperature-programmed reaction in isobutene (100-600 °C, 2 °C/min, He/O$_2$/C$_4$H$_8$/H$_2$O = 70/14/8/8 vol.%) at Mo K- (a), Bi L$_3$- (b), Co K- (c) and Fe K-edge (d).
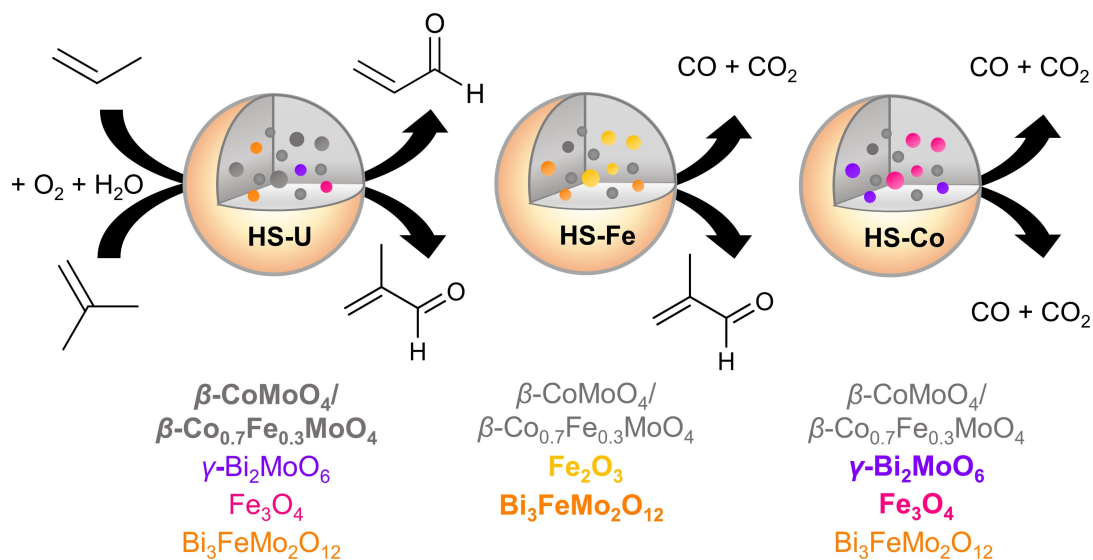
Figure 9. Schematic illustration of the metal oxide phase composition of the *in situ* activated catalysts and their influence on selectivity in selective propylene and isobutene oxidation. Metal oxide phases written in bold refer to the main phases in relation to the other catalyst compositions.

Conclusions

Three selected Bi—Mo—Co—Fe—O catalysts with varying elemental ratios were prepared by hydrothermal synthesis at pH = 7. Their catalytic performance and structure strongly impacted the selective propylene and isobutene oxidation. Due to the high complexity of the 4-component system, advanced complementary characterization methods were required in addition to lab-reactor tests and *ex situ* characterization. These included *operando* Raman spectroscopy, synchrotron XRD and multi-edge XAS. Synchrotron XRD was especially powerful for deconvoluting the complex metal oxide phase mixtures due to the high S/N ratio and small instrumental line broadening.

In general, the catalytic performance of the Bi—Mo—Co—Fe-oxides was only at certain metal ratios superior to previously reported 2-component systems (Bi—Mo—O). This was traced back to the specific metal oxide phases present in each catalyst, which depended on the applied synthesis conditions. Despite the different metal ratios used during synthesis, the as-prepared catalysts exhibited rather similar phase ensembles, which underline the pH sensitivity of HS. However, the metal oxide phase evolution during reaction differed within each system and thus influenced their catalytic performance in lower olefin oxidation.

The direct comparison of the structural changes during either selective propylene or isobutene oxidation revealed the same metal oxides phases in both reactions. In accordance with previous findings in selective isobutene oxidation, the synergistic interplay of Fe_3O_4 and γ-Bi_2MoO_6 also tended towards total oxidation of propylene. On the other hand, lower amounts of Fe_3O_4 in combination with γ-Bi_2MoO_6 improved the catalytic performance in both propylene and isobutene oxidation. This proves the relevance of individual phase amounts present, in addition to overall metal composition. The most pronounced differences in catalytic behaviour were observed for the interplay of Fe_2O_3 and $Bi_3FeMo_2O_{12}$, which showed poor activity and selectivity in propylene oxidation, but highly active and selective performance in isobutene oxidation. Hence, the consideration of bismuth molybdates as key active phases in lower olefin oxidation seems to apply for selective propylene oxidation, while $Bi_3FeMo_2O_{12}$ appears to be equally important in selective isobutene oxidation. This may be related to the higher reactivity of isobutene, a different role of the Fe^{3+}/Fe^{2+} redox couple or different electron/oxygen mobility requirements within the catalyst in each reaction, which should be further addressed in future studies.

Overall, the approach of investigating hydrothermally prepared multi-component systems in the oxidation of lower olefins under comparable conditions by advanced *operando* characterization techniques provided valuable insights into crystalline and amorphous metal oxide phase (trans−)formations, together with information on element specific changes during the catalytic reaction. Such systematic studies should generally be applied for a fundamental understanding of structure-activity correlations in similar but not identical reactions over complex MMOs.

Experimental Section

Catalyst synthesis

Three Bi—Mo—Co—Fe—O catalysts with different elemental composition (Table 3) were prepared by hydrothermal synthesis (HS). The procedure was similar to a previously described one,[39,44] using the precursor masses listed in Table 3. $(NH_4)_6Mo_7O_{24} \cdot 4H_2O$ (Evonik) was solubilized in 40 mL distilled water and stirred for 15 minutes. In parallel, a second solution consisting of $Bi(NO_3)_3 \cdot 6\ H_2O$ (VWR chemicals), $Co(NO_3)_3 \cdot 6\ H_2O$ (Merck) and $Fe(NO_3)_3 \cdot 9\ H_2O$ (VWR chemicals) in 40 mL of nitric acid (2 M) was stirred for 15 min as well. Next, both solutions were combined and adjusted to pH = 7 (pH electrode Titroline easy, Schott instruments) by adding dropwise an aqueous ammonia solution (25 %). After additional 15 minutes of stirring, the suspension was poured into a Teflon inlay and placed in an autoclave (BR-1000, Berghof). The autoclave was heated to 180 °C for 24 hours. Afterwards, the mixture was cooled down to room temperature for further 24 hours. The solid product was separated by filtration (G4 glass frit) and washed with 3x20 mL of deionized water and 3x20 mL of acetone. Afterwards, the solid was dried for 24 hours at room temperature and ultimately calcined in static air for 5 hours at 320 °C.

Catalytic testing

The catalytic testing was performed in a fixed-bed testing unit which is described in refs.[36–37,45] The HS catalysts were ground, pressed and sieved to give a sieve fraction of 300–450 μm. 800 mg of the catalyst were placed in a quartz tubular reactor (i.d. 6 mm) and heated to 180 °C (5 °C/min) in synthetic air (N_2/O_2 = 80/20 vol.%, 100 mL/min) for preconditioning. For selective propylene oxidation ($N_2/O_2/C_3H_6/H_2O$ = 70/14/8/8 vol %, ~1 atm), each catalyst was tested in a temperature range of 360–450 °C (2 °C/min) at a total flow of 100 mL/min (WHSV 1.14 h^{-1}). For selective isobutene oxidation ($N_2/O_2/C_4H_8/H_2O$ = 70/14/8/8 vol %, ~1 atm), each catalyst was tested in a temperature range of 330–390 °C (2 °C/min) at a total flow of 75 mL/min (WHSV 1.17 h^{-1}). For each condition, the oven temperature was kept constant for at least 3 h until a stable conversion level was achieved as monitored by an on-line oxygen sensor (PAROX 1200 H, MBE AG). Subsequently, GC data were acquired and from the resulting chromatograms, conversion and selectivity were calculated. The equations for calculation of olefin conversion and product selectivity are given in the ESI, section 2.

Ex situ characterization

The *ex situ* characterization of the catalysts was conducted by inductively coupled plasma optical emission spectrometry (ICP-OES), N_2-physisorption, Raman spectroscopy and synchrotron XRD before and after catalytic testing in selective olefin oxidation.

The elemental composition was measured by ICP-OES with an iCAP 7600 DUO (Thermo Fisher Scientific) after dissolving 50 mg sample in 6 mL HCl, 2 mL HNO_3 and 1 mL H_2O_2 through heating in a microwave for 45 min at 600 W. The specific surface area of the catalysts was determined by N_2-physisorption at −196 °C using a BELSORP mini-II (MicrotracBEL) and calculated *via* the Brunauer-Emmett-Teller (BET) method[55] in the p/p_0 = 0.05–0.3 range. Prior to the measurements, the samples were heated in vacuum at 300 °C for 2 h. *Ex situ* Raman spectroscopy was measured with an inVia Raman spectrometer (Renishaw) equipped with a frequency doubled Nd:YAG laser (532 nm, 100 mW) and an optical microscope (Leica). An area of at least 200×150 μm² (~20.000 spectra) with a raster size of 1.3 μm was scanned using a line shaped laser (1 % laser intensity, 30 s acquisition time, 2400 lines/mm grating,

ChemCatChem

Research Article
doi.org/10.1002/cctc.202301470

Chemistry Europe
European Chemical
Societies Publishing

spectral range of 60–1320 cm^{-1}). Data treatment was done with WiRE 4.4 (Renishaw). *Ex situ* synchrotron XRD was measured at the beamline P02.1 (DESY, Hamburg, Germany). XRD patterns were acquired using a Varex XRD 4343CT detector and monochromatic beam ($\lambda = 0.20735$ Å). Azimuthal integration of the acquired 2D images was done with the *pyFAI* package.[56] A LaB$_6$ reference was measured for sample to detector distance calibration and to retrieve an instrumental profile function. Rietveld refinement ($2\theta = 1$–$10°$) was performed using TOPAS (v.6, Bruker AXS),[57] with references available in the Inorganic Crystal Structure Database (ICSD, see ESI Table S5).

Operando characterization

The *operando* characterization by synchrotron-based XAS, XRD and laboratory-based Raman spectroscopy was performed in a fixed-bed microreactor setup.[58] 7 mg catalyst with a sieve fraction of 100–200 μm (undiluted for XRD, Raman spectroscopy; transmission adjusted and thus diluted with α-Al$_2$O$_3$ in a ratio of 1:4 (m/m) for XAS) was filled into a 1 mm thick quartz capillary (10 μm wall thickness, WJM-Glas Müller GmbH). For each experiment, the same gas mixture (propylene oxidation: He/O$_2$/C$_4$H$_8$/H$_2$O = 70/14/8/8 vol%; isobutene oxidation: He/O$_2$/C$_4$H$_8$/H$_2$O = 70/14/8/8 vol%; total flow 10 mL/min) and temperature program (100-600 °C, 2 °C/min) were applied. The temperature inside the capillary was calibrated by an inserted type K thermocouple, thus considering the individual heating efficiency of the gas blower (LE MINI SENSOR KIT, Leister Technologies). For the *operando* XRD studies, the temperature was calibrated by the thermal lattice expansion of a silver reference. Dosage of the gases propylene (N25, Air Liquide), isobutene (N25, Air Liquide), oxygen (N48, Air Liquide) and helium (N50, Air Liquide) was achieved by mass flow controllers (Bronkhorst) with water vapor dosed through a self-built heated steel saturator. To avoid water and product condensation, all gas lines were heated to 200 °C. The gas mixture was analysed by an on-line mass spectrometer (OMNI Star GSD 320, Pfeiffer Vacuum) and the unique fragments of each product species are shown in the mass spectra.

Operando XAS experiments at Mo K-, Bi L$_3$-, Co K- and Fe K-edges in transmission mode were performed at ROCK beamline (SOLEIL, Saint-Aubin, France). The unique setup available at ROCK enables fast edge changing,[59–60] and thus the acquisition of all absorption edges during a single run based on alternate use of two monochromators. For data acquisition at Mo K-edge, the Si(220) monochromator was used and for the Bi L$_3$-, Co K-, and Fe K-edges a Si(111) monochromator. XAS data was acquired in the middle of the catalyst bed at 2 Hz in the continuous scanning mode (QEXAFS). To acquire data for all metals in a single experiment, a loop in the sequence of Mo K-, Bi L$_3$- and Fe K-/Co K-edge (recorded in a single scan) was performed. One complete acquisition loop during heating lasted around 6 minutes, with 25 s acquisition at Mo K-, 60 s at Bi L$_3$- and 180 s at Fe K/Co K-edges. XAS spectra of the initial and final state of the catalysts (before and after heating) were recorded under He atmosphere at 100 °C. At constant temperature, acquisition at Mo K-edge lasted 300 s, whereas at Bi L$_3$- and Fe K-/Co K-edges it lasted 600 s each. The spectra of one acquisition period were averaged to produce a single spectrum for each edge. Energy calibration, averaging, background subtraction, and normalization were conducted with the beamline software.[61] Further data treatment (*e.g.*, LCF) was performed with the software package IFEFFIT.[62] More details on XAS data acquisition and analysis can be found in the ESI, section 3.2.

Operando Raman spectroscopy was performed with an inVia Raman spectrometer (Renishaw) equipped with a frequency doubled Nd:YAG laser (532 nm, ~100 mW at the source). Raman spectra were measured with 50 % laser intensity, 120 s acquisition time and 2400 lines/mm grating resulting in a spectral range of 60–1320 cm^{-1}. To avoid detecting potential local heterogeneities of the Bi–Mo–Co–Fe-oxides with different sensitivities of the individual metal oxide phases, the Raman optics was moved periodically (1 period/min) and parallel to the capillary centre (+/−0.3 mm) to detect the metal oxide phases present on average. Data treatment including cosmic ray removal, noise filtering, truncation and baseline subtraction was performed with WiRE 4.4 (Renishaw). Assignment of Raman bands was based on the references given in the ESI, Table S6.

Operando XRD experiments were performed at the Swiss-Norwegian beamline (SNBL) BM01 (ESRF, Grenoble, France). XRD patterns were acquired with the PILATUS@ SNBL diffractometer,[63] including a Pilatus 2 M detector (Dectris) and monochromatic beam ($\lambda = 0.63988$ Å, 300×300 μm^2). Azimuthal integration of the acquired 2D images was done with Bubble software.[63] XRD patterns were recorded in the middle of the catalyst bed with 30 s acquisition time. Additionally, a LaB$_6$ reference was measured for sample to detector distance calibration and to retrieve an instrumental profile function. Sequential Rietveld refinement ($2\theta = 2.5$–$27.5°$) was performed using TOPAS (v.6, Bruker AXS),[57] with references available in the Inorganic Crystal Structure Database (ICSD, Table S5). Data analysis is described in detail in the ESI, section 3.3.

Supporting Information

The authors have cited additional references within the Supporting Information.[36–37,45,47,57,61–62,64–94]

Conflict of Interests

The authors declare no conflict of interest.

Data Availability Statement

The data that support the findings of this study are available from the corresponding author upon reasonable request.

[1] J. Haber, in *Handbook of Heterogeneous Catalysis* (Eds.: G. Ertl, H. Knözinger, F. Schüth, J. Weitkamp), Wiley-VCH, Weinheim, **2008**, pp. 3359–3384.

[2] D. Arntz, A. Fischer, M. Höpp, S. Jacobi, J. Sauer, T. Ohara, T. Sato, N. Shimizu, H. Schwind, in *Ullmann's Encyclopedia of Industrial Chemistry, Vol. 1*, Wiley-VCH, Weinheim, **2007**, pp. 329–346.

[3] R. K. Grasselli, J. D. Burrington, in *Handbook of Heterogeneous Catalysis* (Eds.: G. Ertl, H. Knözinger, F. Schüth, J. Weitkamp), Wiley-VCH, Weinheim, **2008**, pp. 3479–3489.

[4] G. Centi, F. Cavani, F. Trifirò, in *Selective Oxidation by Heterogeneous Catalysis*, Springer, Boston, MA, **2001**, pp. 1–24.

[5] P. Sprenger, W. Kleist, J.-D. Grunwaldt, *ACS Catal.* **2017**, *7*, 5628–5642.

[6] R. K. Grasselli, *Top. Catal.* **2002**, *21*, 79–88.

[7] G. W. Keulks, L. D. Krenzke, T. M. Notermann, *Adv. Catal.* **1979**, *27*, 183–225.

[8] R. K. Grasselli, *Catal. Today* **2014**, *238*, 10–27.

[9] Y. Moro-Oka, W. Ueda, *Adv. Catal.* **1994**, *40*, 233–273.

[10] J. L. Callahan, R. K. Grasselli, E. C. Milberger, H. A. Strecker, *Ind. Eng. Chem. Prod. Res. Dev.* **1970**, *9*, 134–142.

[11] A. T. Bell, *J. Catal.* **2022**, *408*, 436–452.

[12] D. Carson, G. Coudurier, M. Forissier, J. C. Védrine, A. Laarif, F. Theobald, *J. Chem. Soc. Faraday Trans. 1* **1983**, *79*, 1921–1929.

[13] J. R. Monnier, G. W. Keulks, *J. Catal.* **1981**, *68*, 51–66.

[14] J. F. Brazdil, D. D. Suresh, R. K. Grasselli, *J. Catal.* **1980**, *66*, 347–367.

[15] L. D. Krenzke, G. W. Keulks, *J. Catal.* **1980**, *64*, 295–302.

[16] J. D. Burrington, R. K. Grasselli, *J. Catal.* **1979**, *59*, 79–99.

[17] J. F. Brazdil, *Appl. Catal. A* **2017**, *543*, 225–233.

[18] K. Amakawa, J. M. Mauss, P. Müller, B. Hinrichsen, S. Hirth, A. Bader, S. W. T. Price, S. D. Jacques, J. Macht, *Sci. Adv.* **2023**, *9*, eadh5331.

[19] M. Tanimoto, H. Yunoki, H. Hironaka, N. Kuimura, *Vol. EP1074538 A2*, Nippon Shokubai Co Ltd, European Union, **2000**.

[20] H. Martan, U. Wegerle, W. Ruppel, L. Riekert, D. Becker, M. Kotter, *Vol. US00514409 A*, BASF Aktiengesellschaft, United States, **1992**.

[21] K. Schuh, W. Kleist, M. Høj, V. Trouillet, P. Beato, A. D. Jensen, J.-D. Grunwaldt, *Catalysts* **2015**, *5*, 1554–1573.

[22] G. W. Keulks, J. L. Hall, C. Daniel, K. Suzuki, *J. Catal.* **1974**, *34*, 79–97.

[23] F. Trifiro, H. Hoser, R. D. Scarle, *J. Catal.* **1972**, *25*, 12–24.

[24] M. Le, van Craenenbroeck, I. van Driessche, S. Hoste, *Appl. Catal. A* **2003**, *249*, 355–364.

[25] M. T. Le, W. J. van Well, I. van Driessche, S. Hoste, *Can. J. Chem. Eng.* **2005**, *83*, 336–343.

[26] R. P. Rastogi, A. K. Singh, C. S. Shukla, *J. Solid State Chem.* **1982**, *42*, 136–148.

[27] G. R. Patzke, Y. Zhou, R. Kontic, F. Conrad, *Angew. Chem. Int. Ed. Engl.* **2011**, *50*, 826–859.

[28] A. Trunschke, G. Bellini, M. Boniface, S. J. Carey, J. Dong, E. Erdem, L. Foppa, W. Frandsen, M. Geske, L. M. Ghiringhelli, F. Girgsdies, R. Hanna, M. Hashagen, M. Hävecker, G. Huff, A. Knop-Gericke, G. Koch, P. Kraus, J. Kröhnert, P. Kube, S. Lohr, T. Lunkenbein, L. Masliuk, R. Naumann d'Alnoncourt, T. Omojola, C. Pratsch, S. Richter, C. Rohner, F. Rosowski, F. Rüther, M. Scheffler, R. Schlögl, A. Tarasov, D. Teschner, O. Timpe, P. Trunschke, Y. Wang, S. Wrabetz, *Top. Catal.* **2020**, *63*, 1683–1699.

[29] H. Li, K. Li, H. Wang, *Mater. Chem. Phys.* **2009**, *116*, 134–142.

[30] Y. Shi, S. Feng, C. Changsheng, *Mater. Lett.* **2000**, *44*, 215–218.

[31] A. M. Beale, G. Sankar, *Chem. Mater.* **2003**, *15*, 146–153.

[32] K. Schuh, W. Kleist, M. Høj, V. Trouillet, P. Beato, A. D. Jensen, G. R. Patzke, J.-D. Grunwaldt, *Appl. Catal. A* **2014**, *482*, 145–156.

[33] C. Kongmark, R. Coulter, S. Cristol, A. Rubbens, C. Pirovano, A. Löfberg, G. Sankar, W. van Beek, E. Bordes-Richard, R.-N. Vannier, *Cryst. Growth Des.* **2012**, *12*, 5994–6003.

[34] R. Krabetz, *Chem. Ing. Tech.* **1974**, *46*, 1029–1041.

[35] O. V. Udalova, D. P. Shashkin, M. D. Shibanova, O. V. Krylov, *Kinet. Catal.* **2008**, *49*, 407–412.

[36] M. Stehle, A. Gaur, S. Weber, T. L. Sheppard, M. Thomann, A. Fischer, J.-D. Grunwaldt, *J. Catal.* **2022**, *408*, 339–355.

[37] L. Klag, A. Gaur, M. Stehle, S. Weber, T. L. Sheppard, J.-D. Grunwaldt, *ACS Catal.* **2023**, *13*, 14241–14256.

[38] L. Klag, T. L. Sheppard, J.-D. Grunwaldt, *ChemCatChem* **2023**, *15*, e202201276.

[39] P. Sprenger, J.-D. Grunwaldt, W. Kleist, A. Fischer, *Vol. EP3219386 A1* (Ed.: E. P. Office), EU, **2017**.

[40] A. Trunschke, in *Chemical Energy Storage*, 2 ed., De Gruyter, **2022**, pp. 301–368.

[41] A. Rabenau, *Angew. Chem. Int. Ed.* **1985**, *24*, 1026–1040.

[42] G. Ganzer, H. Freund, *Ind. Eng. Chem. Res.* **2019**, *58*, 1857–1874.

[43] M. Stehle, T. L. Sheppard, M. Thomann, A. Fischer, H. Besser, W. Pfleging, J.-D. Grunwaldt, *Catal. Sci. Technol.* **2021**, *11*, 5781–5790.

[44] P. Sprenger, M. Stehle, A. Gaur, J. Weiß, D. Brueckner, Y. Zhang, J. Garrevoet, J.-P. Suuronen, M. Thomann, A. Fischer, J.-D. Grunwaldt, T. L. Sheppard, *ChemCatChem* **2021**, *13*, 2483–2493.

[45] P. Sprenger, M. Stehle, A. M. Gänzler, D. Gashnikova, W. Kleist, J.-D. Grunwaldt, *ACS Catal.* **2018**, *8*, 6462–6475.

[46] J. F. Brazdil, *Catal. Sci. Technol.* **2015**, *5*, 3452–3458.

[47] J. Engeldinger, J. Radnik, C. Kreyenschulte, F. Devred, E. M. Gaigneaux, A. Fischer, H. W. Zanthoff, U. Bentrup, *ChemCatChem* **2016**, *8*, 976–983.

[48] Y. Moro-Oka, W. Ueda, K.-H. Lee, *J. Mol. Catal. A* **2003**, *199*, 139–148.

[49] A. Sleight, W. Jeitschko, *Mater. Res. Bull.* **1974**, *9*, 951–954.

[50] J. A. Rodriguez, S. Chaturvedi, J. C. Hanson, A. Albornoz, J. L. Brito, *J. Phys. Chem. B* **1998**, *102*, 1347–1355.

[51] C. Stewart, E. K. Gibson, K. Morgan, G. Cibin, A. J. Dent, C. Hardacre, E. V. Kondratenko, V. A. Kondratenko, C. McManus, S. Rogers, C. E. Stere, S. Chansai, Y. C. Wang, S. J. Haigh, P. P. Wells, A. Goguet, *ACS Catal.* **2018**, *8*, 8255–8262.

[52] D. Decarolis, A. H. Clark, T. Pellegrinelli, M. Nachtegaal, E. W. Lynch, C. R. A. Catlow, E. K. Gibson, A. Goguet, P. P. Wells, *ACS Catal.* **2021**, *11*, 2141–2149.

[53] D. Espinoza, B. Wollak, T. L. Sheppard, A. C. Dippel, M. Sturm, O. Gutowski, M. Schmidt, O. Korup, R. Horn, *ChemCatChem* **2022**, *14*, e202200337.

[54] B. Wollak, D. E. Doronkin, D. Espinoza, T. Sheppard, O. Korup, M. Schmidt, S. Alizadefanaloo, F. Rosowski, C. Schroer, J.-D. Grunwaldt, R. Horn, *J. Catal.* **2022**, *408*, 372–387.

[55] S. Brunauer, P. H. Emmett, E. Teller, *J. Am. Chem. Soc.* **1938**, *60*, 309–319.

[56] J. Kieffer, V. Valls, N. Blanc, C. Hennig, *J. Synchrotron Radiat.* **2020**, *27*, 558–566.

[57] A. A. Coelho, *J. Appl. Crystallogr.* **2018**, *51*, 210–218.

[58] J.-D. Grunwaldt, M. Caravati, S. Hannemann, A. Baiker, *Phys. Chem. Chem. Phys.* **2004**, *6*, 3037–3047.

[59] V. Briois, C. La Fontaine, S. Belin, L. Barthe, T. Moreno, V. Pinty, A. Carcy, R. Girardot, E. Fonda, *J. Phys. Conf. Ser.* **2016**, *712*, 012149.

[60] C. La Fontaine, S. Belin, L. Barthe, O. Roudenko, V. Briois, *Synchrotron Radiat. News* **2020**, *33*, 20–25.

[61] C. Lesage, E. Devers, C. Legens, G. Fernandes, O. Roudenko, V. Briois, *Catal. Today* **2019**, *336*, 63–73.

[62] B. Ravel, M. Newville, *J. Synchrotron Radiat.* **2005**, *12*, 537–541.

[63] V. Dyadkin, P. Pattison, V. Dmitriev, D. Chernyshov, *J. Synchrotron Radiat.* **2016**, *23*, 825–829.

[64] G. Smith, J. Ibers, *Acta Crystallogr.* **1965**, *19*, 269–275.

[65] P. Adamski, D. Moszynski, A. Komorowska, M. Nadziejko, A. Sarnecki, A. Albrecht, *Inorg. Chem.* **2018**, *57*, 9844–9850.

[66] H. Ehrenberg, I. Svoboda, M. Wiesmann, H. Weitzel, *Acta Crystallogr. Sect. C* **1999**, *55*, 1383–1384.

[67] J. P. Picard, G. Baud, J. P. Besse, R. Chevalier, *J. Less-Common Met.* **1980**, *75*, 99–104.

[68] A. Van den Elzen, G. Rieck, *Acta Crystallogr. Sect. B* **1973**, *29*, 2433–2436.

[69] H.-Y. Chen, A. W. Sleight, *J. Solid State Chem.* **1986**, *63*, 70–75.

[70] F. Pertlik, J. Zeman, *Fortschr. Mineral.* **1982**, *60*, 162–163.

[71] G. Malmros, *Acta Chem. Scand.* **1970**, *24*, 384–396.

[72] A. W. Sleight, B. L. Chamberland, J. F. Weiher, *Inorg. Chem.* **1968**, *7*, 1093–1098.

[73] M. Rapposch, J. Anderson, E. Kostiner, *Inorg. Chem.* **1980**, *19*, 3531–3539.

[74] M. Fleet, *Acta Crystallogr. Sect. B* **1981**, *37*, 917–920.

[75] W. Jeitschko, A. Sleight, W. McClellan, J. Weiher, *Acta Crystallogr. Sect. B* **1976**, *32*, 1163–1170.

[76] T. Leisegang, A. Levin, J. Walter, D. Meyer, *Cryst. Res. Technol.* **2005**, *40*, 95–105.

[77] L. Kihlborg, *Ark. Kemi* **1964**, *21*, 443–460.

[78] E. Payen, M. Dhamelincourt, P. Dhamelincourt, J. Grimblot, J. Bonnelle, *Appl. Spectrosc.* **1982**, *36*, 30–37.

[79] S. S. Saleem, *Infrared Phys.* **1987**, *27*, 309–315.

[80] R. K. S. Costa, S. C. Teles, K. P. F. Siqueira, *Chem. Pap.* **2021**, *75*, 237–248.

[81] V. G. Hadjiev, M. Iliev, I. Vergilov, *J. Phys. C* **1988**, *21*, 199–201.

[82] T. D. Sparks, A. Gurlo, M. F. Bekheet, M. W. Gaultois, G. Cherkashinin, L. Laversenne, D. R. Clarke, *Phys. Rev. B* **2019**, *99*, 104104.

[83] T. C. Peck, C. A. Roberts, G. K. Reddy, *Catalysts* **2020**, *10*, 561–582.

[84] F. D. Hardcastle, I. E. Wachs, *J. Phys. Chem. A* **1991**, *95*, 10763–10772.

[85] F. D. Hardcastle, I. E. Wachs, *J. Solid State Chem.* **1992**, *97*, 319–331.

[86] H. Tian, I. E. Wachs, L. E. Briand, *J. Phys. Chem. B* **2005**, *109*, 23491–23499.

[87] V. D'Ippolito, G. B. Andreozzi, D. Bersani, P. P. Lottici, *J. Raman Spectrosc.* **2015**, *46*, 1255–1264.

[88] W. Sears, W. Keeler, *Appl. Spectrosc.* **1992**, *46*, 1898–1903.

[89] L. Seguin, M. Figlarz, R. Cavagnat, J.-C. Lassègues, *Spectrochim. Acta Part A* **1995**, *51*, 1323–1344.

[90] R. J. Thibeau, C. W. Brown, R. H. Heidersbach, *Appl. Spectrosc.* **1978**, *32*, 532–535.

[91] D. Balzar, in *Microstructure Analysis from Diffraction, Vol. 10* (Eds.: R. L. Snyder, H. J. Bunge, J. Fiala), International Union of Crystallography, **1999**, pp. 94–126.

[92] R. E. Dinnebier, A. Leineweber, J. S. O. Evans, *Rietveld refinement: practical powder diffraction pattern analysis using TOPAS*, Walter de Gruyter GmbH & Co KG, **2018**.

[93] J. S. O. Evans, *Mater. Sci. Forum* **2010**, *651*, 1–9.

[94] J. S. O. Evans, http://topas.dur.ac.uk/topaswiki/doku.php?id=topas (accessed 16/07/2023).